Journal of Materials Chemistry A

Accepted Manuscript

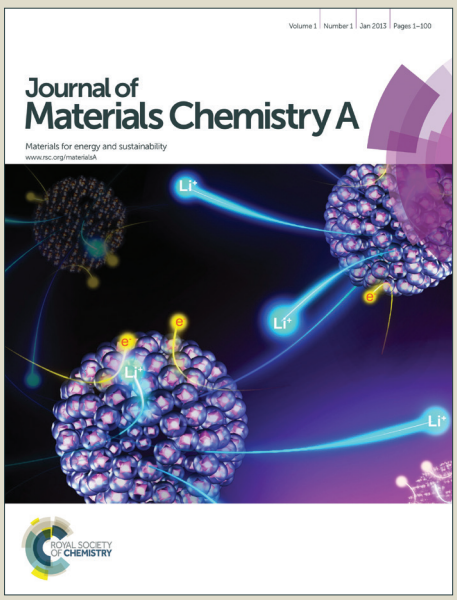

ROYAL SOCIETY OF CHEMISTRY

www.rsc.org/materialsA

Journal of Materials Chemistry A

RSCPublishing

ARTICLE

Fluorination of anatase TiO_2 towards titanium oxyfluoride $TiOF_2$: novel synthesis approach and proof of Li-insertion mechanism

Cite this: DOI: 10.1039/xoxxoooooox

Received ooth January 2012,
Accepted ooth January 2012

DOI: 10.1039/xoxxoooooox

www.rsc.org/

N. Louvain,[a,b]*† Z. Karkar,[a,b] M. El-Ghozzi,[a,b] P. Bonnet,[a,b] K. Guérin,[a,b] P. Willmann[c]

Reactivity of pure molecular fluorine F_2 allows the creation of new materials with unique electrochemical properties. We demonstrate that titanium oxyfluoride $TiOF_2$ can be obtained under molecular fluorine from *anatase* titanium oxide TiO_2, while the fluorination of *rutile* TiO_2 leads only to pure fluoride form TiF_4. Contrary to most fluorides, $TiOF_2$ is air-stable and hydrolyses poorly in humid conditions. Such stability makes it possible for $TiOF_2$ to be studied as an electrode material in Li-ion secondary batteries systems. It shows capacities as high as 220 mAh g^{-1} and good cyclability at high current rates at an average potential of 2.3 V vs Li^+/Li. At such a potential, only Li^+ insertion occurs, as proven by *in operando* XRD/electrochemistry experiments.

Introduction

The need for new energy materials has become essential for the development of lithium-ion batteries. Both cathode and anode materials are the purpose of numerous researches all over the world.[1] Titanium oxides are attractive anode energy materials owing to their versatile redox chemistry, relative abundance, and nontoxic nature, and, worth mentioning, they are industrially produced on a wide scale, up to 5 million metric tons worldwide in 2010,[2] as they found many applications, including pigments, sunscreen and UV-absorber, photocatalysis and photovoltaics.[3,4] In theory, they are able to deliver a capacity of 1342.5 mAh g^{-1} upon complete reduction of the metal, and 335.6 mAh g^{-1} when only one lithium ion is considered.

Among different existing TiO_2 structural types (anatase, rutile, brookite, and TiO_2(B)), both anatase and TiO_2(B) present interesting properties with capacities of about 0.5 and 0.8 lithium ion in Li_xTiO_2 at 1.7 and 1.6 V vs Li^+/Li, respectively.[5,6] Most of the electrochemical articles on TiO_2 deal with the anatase phase. However, capacities of anatase are limited by a phase transition occurring at x = 0.5 that greatly reduces lithium diffusion, while no such transition occurs in TiO_2(B), and nanostructuration has recently emerged as a way to improve their capacities.[6] Some recent reports claim that fluorination of TiO_2 is another process that could improve their electrochemical properties,[7-10] as observed for other metal oxide electrode materials.[11-17]

More widely, fluorination of titanium dioxide is poorly documented. Using pure molecular fluorine, the fluorination of a stable phase containing Ti^{4+} should lead to the highest and most stable oxidation state for a titanium (+IV), which is also the highest fluorine content per atom, i.e. TiF_4.[18,19] TiF_4 is a solid at room temperature and a gas for a temperature higher than 284 °C.[20] It is unstable under air and hydrolyses quickly with humidity. However, in some special fluorination conditions such as those used for surface fluorination, an oxyfluoride $TiOF_2$ has been listed.[21] Such $TiOF_2$ is a metastable phase whose thermodynamic data and synthesis conditions are badly mastered. Titanium oxyfluoride $TiOF_2$ is traditionally obtained as a product of hydrolysis of titanium tetrafluoride. It is also prepared by the hydrolysis of titanium trifluorochloride, and from the reaction of aqueous or anhydrous hydrogen fluoride with titanium dioxide.[22-25] It crystallizes with a cubic ReO_3-type structure[24] and it is a solid up to 450 °C, stable under air.[26]

Titanium fluorides or oxyfluorides have not yet been thoroughly investigated as electrode materials because of the instability of

TiF_4 under air and the low-related electrochemical performances of $TiOF_2$. Indeed a study by Chowdari et al. showed that the $TiOF_2$ structure was destroyed during the first discharge at voltage lower than 1 V in $TiOF_2$/Li half-cells.[27] They proposed that the active material afterwards, which led to capacities as high as 400 mAh g^{-1} (i.e. less than 2 Li^+) between 3.0 and 0.005 V, was in fact amorphous Li_xTiO_y embedded in an a priori inactive LiF matrix, where titanium cannot be oxidized back to its initial +IV state, and this led to a poor cyclability with no plateau.[27] These results can be brought closer to those obtained for electrode materials made of TiF_3, where the formation of an amorphous Li_xTiF_y/LiF composite could display capacities of 600 mAh g^{-1} with voltage profiles similar to the previous Li_xTiO_y/LiF composite.[28,29] Some authors have also reported that amorphous composites of Li_xTiO_y/TiF_3/LiF could show capacities up to 400 mAh g^{-1} but with the lack of reversibility because of a too low potential cutoff.[10] It seems clear that for further electrochemical investigation, some effort must be made in order to work in an electrochemical window of 3-1 V vs Li^+/Li to maintain the initial structure. Even though reversible chemical lithiation of $TiOF_2$ seems feasible up to 0.5 lithium ion per formula unit,[30] no report of electrochemical Li-(de)insertion is to be found yet.

Going further on getting a pure $TiOF_2$ structure and working on electrochemical process that does not alter its pristine structure (insertion-like mechanism) appears as a challenging objective in order to clearly determine the potentiality of $TiOF_2$. The most practical fluorination technique to get pure $TiOF_2$ is a gas-solid fluorination with pure molecular fluorine.[18,31] The main advantage of such fluorination process is the absence of solvent: the reactant can be thermally activated under vacuum in order to avoid any residual pollutant on the crystal surface that could interact with F_2 gas prior to the synthesis and therefore lead to impurities. Indeed surface pollution of inorganic oxyfluorides synthesized through aqueous media is a known and recurrent problem.[32] Here it is demonstrated that $TiOF_2$ can be successfully synthesized by gas-solid fluorination of anatase TiO_2 under pure molecular fluorine F_2. By optimizing synthesis conditions in terms of phases and nanostructuration, it is possible to maximize the reaction yield. Then, the obtained materials have been fully characterized by XRD, TGA, SEM and Raman. Their electrochemical properties as electrode in secondary lithium battery has been determined at different current densities and, focusing on an insertion process, this electrochemical mechanism has been studied through *in operando* XRD measurements.

Experimental

Materials and methods

Anatase (nanopowder, <25 nm particle size, 99.7%, specific surface area 45-55 m^2/g) and rutile (micropowder ≥99%) TiO_2 phases have been purchased from Sigma-Aldrich, and anatase TiO_2 (micropowder ≥99%) from Fluka. All powders were used without further purification. Pure molecular fluorine F_2 gas (98-99%, 27 bars) has been purchased from Solvay Chemicals, Solvay Fluor GmbH, Germany. The fluorinated products have been stored and handled in an argon-filled glovebox with a humidity level below 0.05 ppm.

Thermodynamic simulations

Calculations have been run through the Fact-Web interface of the FactSage package. The fluorination system has been simulated by taking into account one mole of TiO_2 at 1 atm. The system is closed and the Gibbs energy minimized. The simulation is run on a database that contains most thermodynamically stable phases, from which certain metastable phases may be absent.

Titanium oxide fluorination

Anatase and rutile TiO_2 phases have been fluorinated under a mixture of pure molecular fluorine and nitrogen gas at 25 and 250 °C. Direct F_2-gas fluorination process was performed in dedicated fluorine equipment using special handling procedures. A cylindrical nickel reactor of approx. 50 cm in length and offering a volume of approx. 1 litre was used for the reaction. The heating was ensured by a horizontal tubular oven surrounding the reactor, with a domain of homogeneous temperature of approx. 10 cm. All samples were set in a passivated nickel boat. Approximately 1 g (12.52 mmol) of titanium oxide is placed on a passivated nickel boat, and the powder surface exposed to the reactive atmosphere is manually limited to 8-10 cm^2, which induced a thickness of the powdered deposit of a few millimetres. The boat was placed at the centre of the fluorination oven, which was first evacuated in order to reach a relative pressure about -960 mbar. This step ensures the removal of adsorbed water molecules, which may react with F_2 to form HF that may act as catalyst, thus resulting in inhomogeneous fluorination. Then nitrogen and fluorine gases were slowly and successively introduced up to a relative pressure about 0 mbar (i.e. 1 atm) with approximately 450 mbar (13 mmol) of F_2 gas. Then, the temperature is increased to 250 °C with a heating ramp of approximately 2 °C min^{-1} (in the case of room temperature fluorination, the temperature is set to 25 °C). After a desired amount of time (4 to 18 hrs), the system cools down to room temperature, and the reactor oven is flushed with nitrogen gas for 1 hr.

Solid-state characterizations

X-ray powder diffraction (XRPD). XRPD experiments have been carried out on a PANalytical X-Pert Pro diffractometer equipped with a diffracted beam monochromator Cu Kα source and an X'celerator linear detector by using an environment-controlled cell that allows the data to be collected under a static inert argon atmosphere. The counting time was 200 s and the angle step size 0.0836°.

Thermogravimetry analysis. The thermal behaviour of each precursor and product has been investigated by thermogravimetric analysis under inert argon gas on a Shimadzu TGA-50 thermogravimetric analyser instrument from 25 to 600 °C with a heating ramp of 5 °C.min^{-1}.

Scanning electronic microscopy (SEM). SEM has been carried out on a SUPRA 55VP ZEISS field-effect scanning electron

microscope equipped with a Gemini® column and high efficiency in-lens secondary electron detector. The instrument is fitted with an X-MAX Oxford detector for analytical energy-dispersive X-ray spectroscopy (using the INCA 350 software). EDX analysis was performed at 10 kV acceleration on a wide portion of the sample at an x500 zoom. All samples were coated with graphite prior to the experiment.

Raman spectroscopy. The samples were characterized in solid form by Raman spectroscopy at 514.5 nm (2.41 eV) with a Jobin Yvon T64000 Raman spectrometer.

Galvanostatic charge-discharge measurements

The electrochemical performances of our materials were investigated using galvanostatic discharge-charge cycles. The electrodes were composed of the active material (about 72% by weight, w/w), acetylene black (18% w/w) to ensure the electronic conductivity and polyvinylidene difluoride (PVDF, 10% w/w) as binder. After stirring in propylene carbonate (PC), the mixture was spread uniformly onto a metallic current collector disk of 12 mm in diameter (stainless steel for Swagelok cell type, and Al foil for coin cell type). After the PC evaporation, the electrodes were dried in a vacuum oven at 80 °C overnight to remove traces of adsorbed water and solvent before being transferred into an argon-filled glovebox. The anode was a lithium metal disk, and the separator was Celgard 2034. A two-electrode cell was used (Swagelok cell type, or coin cell type for cyclability measurements) where lithium was both reference and counter electrodes. The C rate calculations were based on the theoretical capacity (263.15 mA g^{-1} for $TiOF_2$, and 335.6 mA g^{-1} for TiO_2). The electrolyte was 1M $LiPF_6$ in propylene carbonate:ethylene carbonate:dimethyl carbonate (PC:EC:3DMC, 1:1:3 vol. %). The cells were assembled in an argon-filled glovebox. Relaxation was performed for at least 5 hours until the open circuit voltage (OCV) stabilization. Galvanostatic discharge-charge cycles were carried out on a VMP2-Z instrument from BioLogic, and were performed at room temperature by applying a constant current in the working region 1.2-3.8 V. Current densities ranging from C/100 to C were used. As a plateau is clearly observed on each galvanostatic curve, the (dis)charge potential is measured at half of the total (dis)charge capacity and is noted $E_{1/2}$.

***Ex situ* XRD/electrochemistry measurements.** The samples studied here were taken from partially or totally discharged Swagelok cells. The cells were cycled at C/10 and prepared according to the procedure described in the article. The discharge was programed to stop at a desired potential (2.5, 2.0 or 1.2 V vs Li^+/Li), and the cells were opened in an argon-filled glovebox. The active material was dried overnight and measured in an environment-controlled cell.

***In operando* XRD/electrochemistry measurements.** The active material preparation for the in operando XRD/electrochemistry measurements is described in the aforementioned procedure, except that the mixture was uniformly spread onto a glass side with a 14-mm diameter. After a vacuum-drying process, the electrode was removed from the glass slide with a scalpel, and placed in an environment-controlled cell. The current collector was composed of an iron-nickel alloy disk with a 12-mm diameter aperture. Celgard 2034 and Whatman glass fibre membranes separate the electrode from the lithium disk. The $TiOF_2$/Li cell was cycled at C/10 for the discharge and at C/20 for the charge (to ensure a complete delithiation). *In operando* XRD/electrochemistry experiments have been carried out by using an environment-controlled cell described in Figure S1. The counting time was 500 s and the angle step size 0.0668°. The measurements were programed and monitored from both XRD and electrochemistry points of view by their respective software. The galvanostatic cycle was set as in a usual measurement, while XRD patterns were constantly collected. In order to closely follow the peak position displacement, the (001) peak of the $TiOF_2$ phase was monitored every 15 min for 2 hrs. After 2 hrs, a wide-range XRD pattern was collected between 10 and 50 °2θ for 40 min. This '8 x 15 min + 40 min' scheme was repeated during the relaxation and the first discharge-charge cycle.

Results and discussion

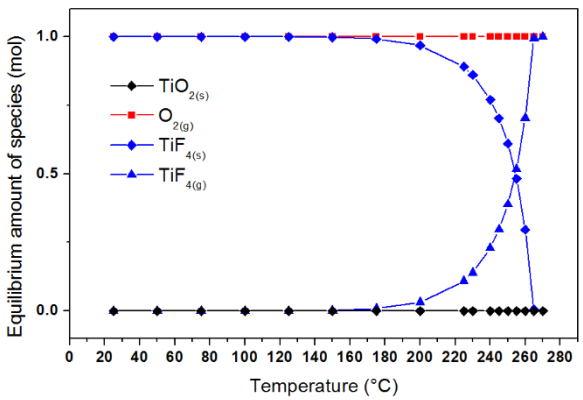

Figure 1. Thermodynamic calculations for various temperatures of a 1:2 ratio of TiO_2:F_2.

According to thermodynamics, the reaction of molecular fluorine F_2 with rutile titanium dioxide TiO_2 at 25 °C should lead to an equimolar mixture of TiF_4 and O_2:

$$TiO_{2(s)} + 2\ F_{2(g)} = TiF_{4(s)} + O_{2(g)} \quad \text{(eq. 1)}$$

From room temperature, the reaction is supposedly quantitative, with solid TiF_4 formed (Figure 1). When the temperature increases, TiF_4 starts to sublimate from approximately 200 °C, and the presence of gaseous TiF_4 becomes non-negligible above 250 °C, which is lower than expected (T_{sub} = 284 °C).[20] The major difficulty is that only TiF_4 is the only stable phase reported and no other, hypothetical or not, metastable fluoride or oxyfluoride phases can be included in the calculation. Moreover the difference of reactivity between anatase and rutile under molecular fluorine has never been analysed. In order to investigate the reactivity of titanium dioxide, anatase and rutile TiO_2 powders have been fluorinated with a mixture of molecular fluorine and nitrogen gases at 250 °C for 18 hours in dedicated fluorination equipment.

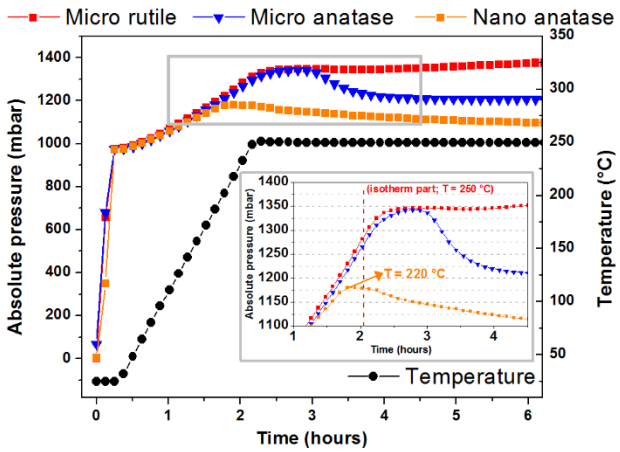

Figure 2. In situ total pressure data collected during static fluorination of rutile and anatase TiO_2 with 1 atm. of a mixture of N_2 and F_2 gases at 250 °C; the inset shows a zoom on the isotherm part of the curves.

Figure 2 displays the results of the *in situ* pressure data collected during the static fluorination process. First, let us consider the case of micrometre-sized powders of rutile and anatase TiO_2. When rutile is heated up to 250 °C in one atm. of a F_2/N_2 mixture, the pressure reaches about 1350 mbar. Then, when temperature is kept at 250 °C, the pressure keeps on slowly increasing. This indicates the formation of a gaseous phase of TiF_4 because of its high tensile strength at such temperature, in good accordance with thermodynamics (Figure 1). On the contrary, when anatase is fluorinated in similar conditions (Figure 2), the pressure profile obtained is clearly dissimilar, suggesting a different reactivity with pure fluorine between both polymorphs, contrary to what was expected. At 250 °C, the pressure drastically decreases from 1350 to 1200 mbar, bespeaking the formation of a new solid phase with a net consumption of F_2 gas. All parameters being kept identical, the only reason for such difference is polymorphism.[33] The first interface encountered by F_2 gas is the crystal surface, thus crystal structure and morphology may affect the reactivity during a gas-solid process.[34] Indeed, such a difference between rutile and anatase is often discussed in adsorption of active species in photocatalysis.

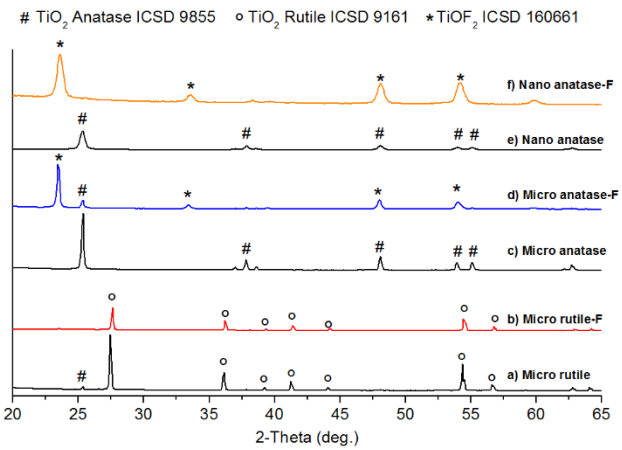

Figure 3. XRD patterns of rutile and anatase TiO_2 precursors and rutile and anatase TiO_2 fluorinated at 250 °C for 18 hrs in static conditions. Characteristic peaks coming from anatase, rutile and cubic $TiOF_2$ are noted.

The XRD patterns of micrometre-sized anatase and rutile TiO_2 fluorinated at 250 °C for 18 hrs are shown in Figure 3. For fluorinated rutile, the XRD signature is characteristic of the rutile phase. This is in good agreement with our conclusions from both the *in situ* pressure data and thermodynamic assumptions: rutile titanium dioxide partially reacts with molecular fluorine to form gaseous titanium tetrafluoride TiF_4, leaving only unreacted rutile TiO_2 at the end of the experiment (Figure 3b). Crystallization of a TiF_4-derived compound, namely $NiTiF_6$, in the cold end of the fluorination oven, where it is very likely that gaseous TiF_4 may have condensed and subsequently reacted with nickel fluoride NiF_2 from the passivation layer of the reactor, is an indirect proof of the formation of gaseous TiF_4 during the fluorination of rutile TiO_2 (Figure S2). Although equimolar quantities of reactants are used, the reaction is not completed after 18 hrs. Etching of rutile with F_2 might be kinetically limited.

When anatase is fluorinated in the same conditions, the resulting powder is unambiguously composed of $TiOF_2$ (Figure 3d), as shown by the intense peaks at $2\theta = 23.4°$, 33.3°, 47.8° and 53.9°, corresponding to (001), (011), (002) and (012) *hkl* planes, respectively (ICSD #160661). Nevertheless peaks from a second minor phase can be identified at $2\theta = 25.3°$, corresponding to (101) *hkl* plane of anatase (ICSD #9855). This reveals that residues of unreacted anatase are still present in the fluorinated powder.

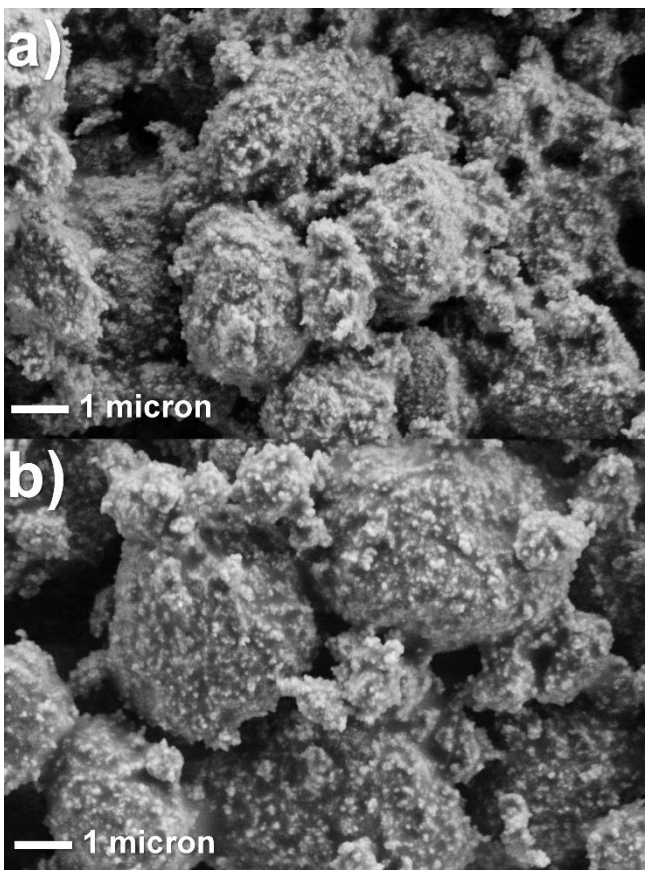

Figure 4. SEM images of anatase (a) and fluorinated anatase (b) nanopowders.

The possibility to isolate $TiOF_2$ from anatase TiO_2 phase being established, crystallite size influence on reactivity can be briefly described. For such purpose, a nanopowder of anatase TiO_2 was fluorinated, as it is known that nanostructuration of fluorides is highly desirable for electrochemical applications.[35] When the

nanosized powder of anatase is heated up to 250 °C under fluorine, the pressure reaches a maximum of 1180 mbar before lessening towards 1100 mbar (Figure 2), that is 100 mbar lower than its microsized parent, indicating both the formation of a new solid phase with a net consumption of F_2 gas and an increased yield. It is noteworthy that the reactivity of nanosized anatase with fluorine is enhanced, as it can be seen from Figure 2. While microsized powders of TiO_2 do not display any unforeseen reactivity before reaching the target temperature of 250 °C, the pressure for nanosized anatase slows down its rise around 175 °C and climbs to its maximum at 220 °C, i.e. 30 °C lower than for the micrometric powders (Figure S3). As for microsized anatase TiO_2, fluorination of nano-anatase leads to $TiOF_2$ (Figure 3f). The resulting powder does not display any peak from its parent anatase phase, indicating that the reaction came close to completion. Interestingly, the crystal size did not suffer from the fluorination conditions, and the initial size of anatase crystals (25 nm) is kept nearly constant after synthesis, and the size of nanocrystals of $TiOF_2$ is approximately 30 nm (Table S1). Figure 4 shows SEM images of nano-anatase before and after fluorination. The pristine powder is composed of sponge-like aggregates, with various sizes larger than 1 µm, made up of self-assembled nanoparticles, and the powder morphology does not seem to have evolved during fluorination.

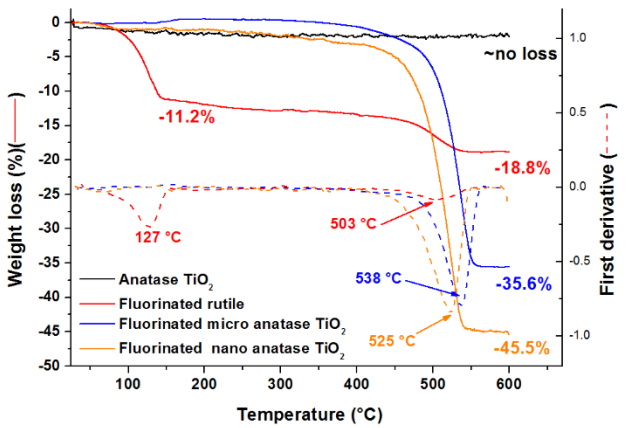

Figure 5. TG profiles of pristine TiO_2 and TiO_2 samples fluorinated at 250 °C for 18 hrs; rutile profile, not shown here, is identical to the anatase one.

Thermogravimetric analyses of pristine and fluorinated titanium dioxide powders are displayed on Figure 5. While neither anatase nor rutile TiO_2 shows any significant loss up to 600 °C, fluorinated rutile decomposes in two steps at 127 and 503 °C and displays weight losses of 11.2 % and 7.6 %, respectively. According to XRD, fluorinated rutile is composed of crystalline rutile TiO_2. The first step might be correlated with the presence of etching product adsorbed on grain surface,[7] while the second step at 503 °C can be attributed to the decomposition of $TiOF_2$ (-7.6 %); the presence of $TiOF_2$ in fluorinated rutile was not evidenced from XRD and may stem from the anatase impurity in the pristine rutile TiO_2 powder (Figure 3a). EDX measurements clearly identified fluorine in fluorinated rutile powder (Figure S4). Fluorinated micrometric anatase is mainly composed of $TiOF_2$ (Figure 3d), and it decomposes in a single step at 538 °C (-35.6 %), leading to anatase TiO_2 (Figure S5). The supposedly higher yield of fluorinated nano-anatase, compared to micro-anatase, is positively demonstrated by the single-step decomposition at 525 °C with an increased weight loss of 45.5 %, a result which is in good accordance with *in situ* pressure data and XRD measurements.

It is commonly accepted that $TiOF_2$ decomposes into equimolar amounts of TiO_2 and TiF_4, which would give rise to a 60 % weight loss.[26] Nonetheless such a value has never been reported, and most of the recent sol-gel derived $TiOF_2$ crystals present weight losses of approximately 30 to 45 %.[9,26] The fact that our $TiOF_2$ nanocrystals do not show a 60 % weight loss, even though their purity is apparently high, may arise from either an incomplete fluorination or a wrong, therefore more complicated, decomposition equation. If the first assumption is considered true, then the Raman spectrum of $TiOF_2$ nanocrystals should reveal the presence of an anatase impurity, which cannot be pinpointed (Figure S6). Consequently, the second assumption must be the right one, and the decomposition pathway of $TiOF_2$ crystals may be more complex than expected.

XRD measurement after thermal treatment shows only the presence of anatase TiO_2 (Figure S5a). Placing a fluorine scavenger such as Li_2CO_3 along with $TiOF_2$ during a thermal treatment up to 600 °C must lead to a 24 % weight loss and to a LiF:TiO_2 mixture in the following proportions:

$$2Li_2CO_{3(s)}+5TiOF_{2(s)}=4LiF_{(s)}+5TiO_{2(s)}+\text{gaseous products} \quad \text{(eq. 2)}$$

Both TG and XRD analyses (Figures S5b-S5c) are in perfect accordance with Equation 2, which does not involve any gaseous titanium fluoride intermediate products. Further investigation by coupled technics with TGA such as mass spectrometry should be made in order to revisit the decomposition products of $TiOF_2$.

We can thus confidently conclude that, based on results from *in situ* pressure data, XRD and TG analyses, 30-nm nanocrystals of pure $TiOF_2$ were obtained from a nanopowder of anatase TiO_2.

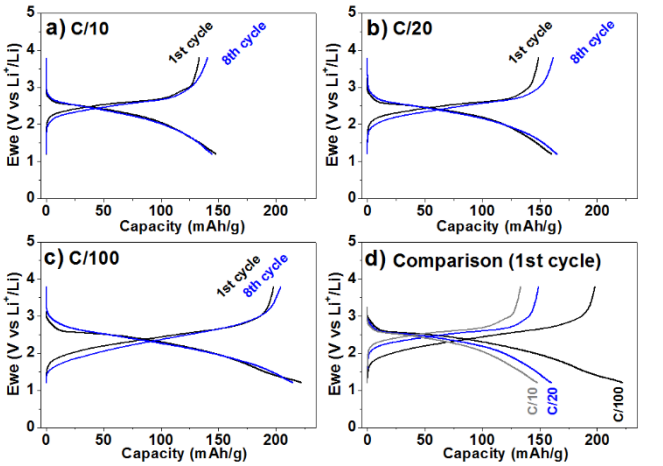

Figure 6. Galvanostatic voltage profiles for $TiOF_2$/Li cells cycled at C/10 (a), C/20 (b), and C/100 (c) between 3.8 and 1.2 V, and a comparison of their first cycle (d).

The as-prepared nanocrystals of $TiOF_2$ were tested as electrode of Li-ion battery in Swagelok-type half-cells. The galvanostatic charge-discharge voltage profiles at three different current rates (C/10, C/20 and C/100, where C is set at 263.15 mAh g^{-1} for a 1-e^- process) of the first and eighth cycles for $TiOF_2$ versus Li between 3.8 and 1.2 V are shown in Figure 6. Such potential window as been chosen according to the studies by Chowdari *et al.*[27] showing that under 1.0 V no more potential plateau occurs in reduction. For each current density, the discharge curves show a relatively flat plateau around 2.25 V vs Li^+/Li. The $TiOF_2$ nanocrystals electrode delivers a reversible specific capacity of

145 mAh g^{-1} at C/10 (Figure 6a) over the first eight cycles. The differences in shape and potential between the first cycle and the following ones are thus relatively small, indicating that the reaction mechanism is most probably the same. At slower rates (Figure 6b-d), the reversible specific capacity is increased up to 155 mAh g^{-1} (C/20) and an impressive 220 mAh g^{-1} (C/100). The fact that the specific capacity increases when reducing the current density would indicate a kinetically limited ionic or electrical diffusion mechanism, which could be explained either by the insulating nature of $TiOF_2$, a common characteristic of fluorinated materials, or a none convenient volume/area ratio of the $TiOF_2$ grains. Noteworthy, the potential of $TiOF_2$ is 0.6 V higher than the one of anatase TiO_2 (Figure S7, Table S2), as expected from the high electronegativity of the fluoride ion.

We endeavoured to study the Li-insertion mechanism into $TiOF_2$ in order to discriminate between a typical insertion, yielding a Li_xTiOF_2 phase, and a conversion reaction, yielding a composite mixture of LiF and Li_yTiO_2 (the formation of Ti^0 in our working potential window has been ruled out). In a first step, an *ex situ* XRD study has been carried out on electrodes that were submitted to a C/10 rate and stopped at 2.5, 2.0, and 1.2 V during their first discharge (Figure S8). The impact of Li-insertion is relatively small on the XRD profile and no lithium fluoride can be detected, thus *a priori* indicating that no conversion reaction may occur in the chosen potential window.

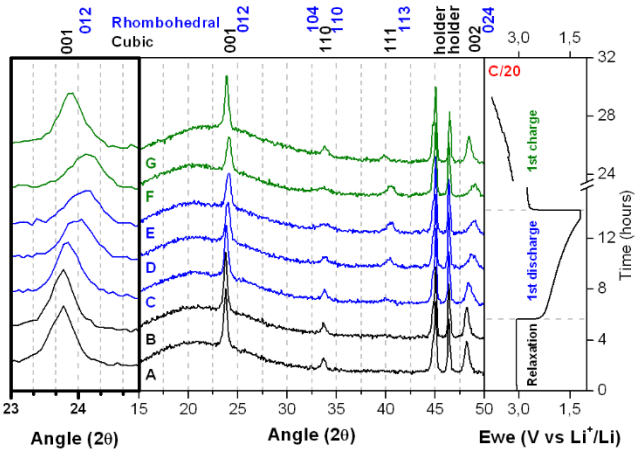

Figure 7. *In operando* evolution of the XRD pattern recorded at C/20 with a close view on the 001 reflection (left) and its corresponding voltage profile (right). Miller indices for the cubic (black) and rhombohedral (blue) cells are shown. Peaks between 45° and 47.5° are originating from the measurement cell.

In order to go further into details in the reaction mechanism of $TiOF_2$ with Li, and to probe cell parameters modulation, the first charge-discharge cycle was investigated by *in operando* XRD and the results are shown in Figure 7. During the open-circuit, only the well-defined peaks of crystalline cubic $TiOF_2$ are visible in the diffraction pattern (Figure 7, patterns A and B) at 2θ = 23.4°, 33.3°, and 47.8°, corresponding to (001), (011), and (002) *hkl* planes, respectively (ICSD #160661), and no evolution, either in intensity or in position, can be detected (Figure S9). At the beginning of the reaction (Figure 7, pattern C), the intensities of these peaks slightly decrease without observing any new peak in the diffraction pattern until half discharge, where Bragg peaks broaden and shift to higher angles (Figure 7, pattern D). This is clearly noticeable on the close view on the 001 reflection (Figure 7 and S10). Please note that at this point of discharge a new peak is unambiguously appearing at 2θ = 40.1°, and that such XRD behaviour is characteristic of Li-intercalation materials.[36] At the end of discharge (Figure 7, pattern E), the set of reflections of the initial cubic $TiOF_2$ phase are broadened and shifted to higher angles, and their intensity is slightly lower. The angle shift may point to the cubic-to-rhombohedral phase transition described for chemically lithiated $TiOF_2$,[30] and the hypothesis has been verified by a profile matching refinement of the fully discharged pattern using a rhombohedral model (*R*-3*c*). All the diffraction features are well modelled by this phase with cell parameters a = 5.206 Å and c = 13.334 Å (Figure S11, Table S3), and this allows us to conclude that the phase at the end of the discharge is a lithiated $TiOF_2$ of general formula Li_xTiOF_2; thus, the present peaks at 2θ = 23.8°, 33.4°, 34.4°, 40.1°, and 48.7° would correspond to (012), (104), (110), (113), and (024) *hkl* planes, respectively. While at the early oxidation process the diffraction pattern can still be indexed by the rhombohedral cell (Figure 7, pattern F), the cubic non-lithiated $TiOF_2$ phase is fully recovered at the end of charge (Figure 7, pattern G), therefore corroborating our hypothesis for Li-insertion and confirming the reversibility of the electrochemical performances obtained. With a concrete picture of the reactions of lithium with titanium oxyfluoride, it is now possible to deduce the lithium content, i.e. x in Li_xTiOF_2 formula, from our electrochemical measurements. At a C/10 rate, a specific capacity of 145 mAh g^{-1} was obtained (Figure 6a) and this leads to a lithiated Li_xTiOF_2 with x = 0.55 (with a theoretical capacity of 263.15 mAh g^{-1} for 1 lithium); the lithium content can be as high as x = 0.87 at C/100, for a specific capacity equal to 220 mAh g^{-1} (Figure 6c).

The Li-insertion mechanism being validated, the cycling performances of our $TiOF_2$ nanocrystals were investigated (Figure 8). The galvanostatic charge-discharge composition-voltage profiles of key cycles of a $TiOF_2$/Li cell consecutively cycled at C/20, C/10, C/20, C, and finally C/20 between 3.8 and 1.2 V are displayed in Figure 8a. The most striking feature of this material is that the specific capacity obtained at C/20 is systematically resumed after being cycled at higher C/10 and C rates. In addition to its excellent cyclic capacity retention at sequential current rates, $TiOF_2$/Li cells demonstrate a stable specific capacity at the high current density of C for more than 30 charge/discharge cycles between 3.0 and 1.2 V (Figure 8b). The discharge capacity slowly increases during the first thirty cycles and reaches 60 mAh g^{-1}. This relatively high capacity retention at C may stem from the presence of O^{2-} ion in $TiOF_2$, which makes it a semiconductor with a band-gap of approximately 2.5 eV,[37] whereas metal fluorides are commonly referred to as insulator with band-gaps larger than 4 eV[38-40] that cannot be cycled at such high density current without nanocarbon grafting.[41-43] An impressive capacity of 200 mAh g^{-1}, close to the theoretical one, can even be obtained when the half-cell is cycled at C/100 (Figure 8b). The system retains a high capacity of 180 mAh g^{-1} after tenth of cycles, a value that can surely be improved by optimizing the battery engineering.

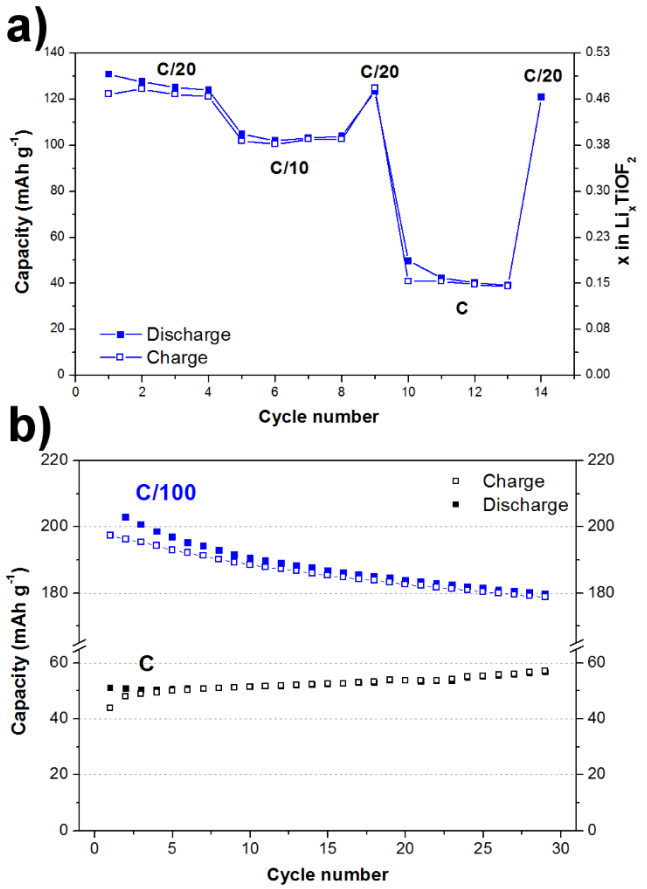

Figure 8. Composition-voltage profiles for one $TiOF_2$/Li cell cycled at C/20, C/10, C/20, C and C/20 consecutively between 3.8 and 1.2 V (a); cycling performance curves of $TiOF_2$ nanocrystals at current densities of C and C/100 (b).

Conclusions

In conclusion, it has been demonstrated that nanocrystals of $TiOF_2$ can successfully be obtained by gas-solid fluorination of TiO_2 anatase nanocrystals, and not from rutile, with molecular fluorine. This material gave us the opportunity to investigate the reaction of lithium with titanium oxyfluoride in $TiOF_2$/Li half-cells. By taking advantage of the different stable oxidation states of Ti ion, in particular Ti^{4+} and Ti^{3+}, it was possible to reversibly intercalate up to 0.87 Li^+ into$TiOF_2$, thus obtaining $Li_{0.87}TiOF_2$. Using *in operando* XRD/electrochemistry, it has been established that $TiOF_2$ can act as a typical Li-insertion material with an average potential of 2.3 V vs Li^+/Li.

Further works will be devoted to the unravelling of the decomposition pathway of $TiOF_2$ by TGA coupled with mass spectrometry, as well as improvements of the electrochemical performances in order to reach the theoretical capacity of 263.15 mAh g^{-1}, by focusing on further nanotexturation and electrode formulation. In the light of such a knowledge regarding the Li-insertion mechanism of $TiOF_2$, its electrochemical performances below 1 V may now be re-investigated.

Acknowledgements

The authors would like to gratefully thank Profs. André Hamwi and Daniel Avignant for fruitful discussions on oxyfluorides, Nicolas Batisse and Lawrence Frezet for the automatized fluorination equipment, Joël Cellier for the development of the *in operando* XRD/electrochemistry cell, and Claire Fonquernie for her global help on all our measurements.

Notes and references

[a] Clermont Université, Université Blaise Pascal, Institut de Chimie de Clermont-Ferrand, BP 10448, F-63000 Clermont-Ferrand, France.
[b] CNRS, UMR 6296, Institut de Chimie de Clermont-Ferrand, F-63177 Aubière, France.
[c] Centre National d'Etudes Spatiales, Toulouse, France.
*Corresponding author. E-mail address: nicolas.louvain@um2.fr. Telephone: +33 4 67 14 33 09. Fax: +33 4 67 14 33 04.
† Present address: Institut Charles Gerhardt UMR CNRS 5253 (AIME), Université Montpellier 2, CC1502, place E. Bataillon, 34095 Montpellier cedex 5, France.

Electronic Supplementary Information (ESI) available: complementary data regarding the synthesis conditions; crystallite size calculations; EDX spectra; complementary TG analyses; Raman spectra; galvanostatic profiles of Li/TiO_2 half-cells; *ex situ* XRD/electrochemistry results, detailed *in operando* XRD/electrochemistry patterns; profile matching refinement of fully discharge Li/$TiOF_2$. See DOI: 10.1039/b000000x/

1. P. G. Bruce, B. Scrosati and J. M. Tarascon, *Angew. Chem. Int. Ed. Engl.*, 2008, **47**, 2930-2946.
2. TDMA, *Cefic - The European Chemical Industry Council*, 2010.
3. G. Bedinger, in *US Geological Survey - Mineral commodity summaries*, 2013, pp. 172-173.
4. X. Chen and S. Mao, *Chem. Rev.*, 2007, **107**, 2891-2959.
5. J.-Y. Shin, D. Samuelis and J. Maier, *Adv. Funct. Mater.*, 2011, **21**, 3464-3472.
6. D. Deng, M. G. Kim, J. Y. Lee and J. Cho, *Energy Environ. Sci.*, 2009, **2**, 818-837.
7. M. Saito, Y. Nakano, M. Takagi, T. Maekawa, A. Tasaka, M. Inaba, H. Takebayashi and Y. Shodai, *Key Eng. Mater.*, 2014, **582**, 127-130.
8. Y. Zeng, W. Zhang, C. Xu, N. Xiao, Y. Huang, D. Y. Yu, H. H. Hng and Q. Yan, *Chem. Eur. J.*, 2012, **18**, 4026-4030.
9. L. Chen, L. Shen, P. Nie, X. Zhang and H. Li, *Electrochim. Acta*, 2012, **62**, 408-415.
10. D. Dambournet, K. Chapman, P. Chupas, R. Gerald, N. Penin, C. Labrugere, A. Demourgues, A. Tressaud and K. Amine, *J. Am. Chem. Soc.*, 2011, **133**, 13240-13243.
11. Z. G. Wang, Z. X. Wang, H. J. Guo, W. J. Peng, X. H. Li and J. X. Wang, *Mater. Lett.*, 2014, **123**, 93-96.
12. K. M. Wiaderek, O. J. Borkiewicz, E. Castillo-Martinez, R. Robert, N. Pereira, G. G. Amatucci, C. P. Grey, P. J. Chupas and K. W. Chapman, *J. Am. Chem. Soc.*, 2013, **135**, 4070-4078.
13. Y. Ma, B. Ding, G. Ji and J. Lee, *ACS Nano*, 2013, **7**, 10870-10878.
14. M. Ati, M. Sougrati, G. Rousse, N. Recham, M. L. Doublet, J. Jumas and J. M. Tarascon, *Chem. Mater.*, 2012, **24**, 1472-1485.
15. Q. Luo, T. Muraliganth and A. Manthiram, *Solid State Ionics*, 2009, **180**, 703-707.
16. K. S. Lee, S. T. Myung, K. Amine, H. YashiroB and Y. K. Sun, *J. Mater. Chem.*, 2009, **19**, 1995-2005.
17. I. D. Gocheva, I. Tanaka, T. Doi, S. Okada and J. Yamaki, *Electrochem Commun*, 2009, **11**, 1583-1585.
18. N. Louvain, A. Fakhry, P. Bonnet, M. El-Ghozzi, K. Guerin, M. T. Sougrati, J. C. Jumas and P. Willmann, *CrystEngComm*, 2013, **15**, 3664-3671.
19. P. Hagenmuller, *Inorganic Solid Fluorides*, Academic Press, Inc., 1985.
20. G. Brauer and G. Brauer, *Handbook of Preparative Inorganic Chemistry*, Academic Press, Inc., 1963.
21. D. Li, H. Haneda, S. Hishita, N. Ohashi and N. Labhsetwar, *J. Fluorine Chem.*, 2005, **126**, 69-77.

22. J. Moss and A. Wright, *J. Fluorine Chem.*, 1975, **5**, 163-167.
23. K. S. Vorres and F. B. Dutton, *J. Am. Chem. Soc.*, 1955, **77**, 2019-2019.
24. K. Vorres and J. Donohue, *Acta Crystallogr*, 1955, **8**, 25-26.
25. H. M. Haendler, S. F. Bartram, R. S. Becker, W. J. Bernard and S. W. Bukata, *J. Am. Chem. Soc.*, 1954, **76**, 2177-2178.
26. S. Xie, X. Han, Q. Kuang, J. Fu, L. Zhang, Z. Xie and L. Zheng, *Chem. Commun.*, 2011, **47**, 6722-6724.
27. M. V. Reddy, S. Madhavi, G. V. Subba Rao and B. V. R. Chowdari, *J. Power Sources*, 2006, **162**, 1312-1321.
28. H. Li, P. Balaya and J. Maier, *J. Electrochem. Soc.*, 2004, **151**, A1878-A1885.
29. H. Li, G. Richter and J. Maier, *Adv. Mater.*, 2003, **15**, 736-739.
30. D. W. Murphy, M. Greenblatt, R. J. Cava and S. M. Zahurak, *Solid State Ionics*, 1981, **5**, 327-330.
31. N. Louvain, J. Peyroux, M. Dubois, W. Simond and F. Leroux, *Inorg. Chem.*, 2014, **53**, 852-860.
32. A. P. Wilkinson, R. E. Josefsberg, L. C. Gallington, C. R. Morelock and C. M. Monaco, *J. Solid State Chem.*, 2014, **213**, 38-42.
33. D. S. Torkhov, P. E. Meskin, Y. V. Kolen'ko, V. A. Ketsko, A. A. Burukhin, B. R. Churagulov and N. N. Oleinikov, *Dokl. Chem.*, 2004, **394**, 36-38.
34. S. C. Li and U. Diebold, *J. Am. Chem. Soc.*, 2010, **132**, 64-66.
35. G. G. Amatucci and N. Pereira, *J. Fluorine Chem.*, 2007, **128**, 243-262.
36. J. N. Reimers and J. R. Dahn, *J. Electrochem. Soc.*, 1992, **139**, 2091-2097.
37. C. Xue, T. Narushima and T. Yonezawa, *J. Inorg. Organomet. Polym.*, 2012, **23**, 239-242.
38. Z. Yang, Y. Pei, X. Wang, L. Liu and X. Su, *Comput. Theor. Chem.*, 2012, **980**, 44-48.
39. R. Li, S. Wu, Y. Yang and Z. Zhu, *J. Phys. Chem. C*, 2010, **114**, 16813-16817.
40. R. E. Doe, K. A. Persson, Y. S. Meng and G. Ceder, *Chem. Mater.*, 2008, **20**, 5274-5283.
41. R. Ma, Y. Dong, L. Xi, S. Yang, Z. Lu and C. Chung, *ACS Appl. Mater. Interfaces*, 2013, **5**, 892-897.
42. C. Li, L. Gu, J. Tong and J. Maier, *ACS Nano*, 2011, **5**, 2930-2938.
43. S. W. Kim, D. H. Seo, H. Gwon, J. Kim and K. Kang, *Adv. Mater.*, 2010, **22**, 5260-5264.

